Three-dimensional-printed gas dynamic virtual nozzles for x-ray laser sample delivery

Garrett Nelson,[1,*] Richard A. Kirian,[1,2] Uwe Weierstall,[1] Nadia A. Zatsepin,[1] Tomáš Faragó,[3] Tilo Baumbach,[3] Fabian Wilde,[4] Fabian B. P. Niesler,[5] Benjamin Zimmer,[5] Izumi Ishigami,[6] Masahide Hikita,[6] Saša Bajt,[7] Syun-Ru Yeh,[6] Denis L. Rousseau,[6] Henry N. Chapman,[2] John C. H. Spence,[1] and Michael Heymann[2,8]

[1]Department of Physics, Arizona State University, Tempe, Arizona 85287, USA
[2]Center for Free Electron Laser Science, Notkestrasse 85, 22607 Hamburg, Germany
[3]Synchrotron Facility ANKA, Karlsruhe Institute of Technology KIT, Hermann-von-Helmholtz-Platz 1, 76344 Eggenstein- Leopoldshafen, Germany
[4]Helmholtz-Zentrum Geesthacht, Max-Planck-Straße 1, 21502 Geesthacht, Germany
[5]Nanoscribe GmbH, Hermann-von-Helmholtz-Platz 1, 76344 Eggenstein-Leopoldshafen, Germany
[6]Department of Physiology and Biophysics, Albert Einstein College of Medicine, Bronx, New York 10461, USA
[7]Photon Science, Deutsches Elektronen-Synchrotron DESY, Notkestraße 85, 22607 Hamburg, Germany
[8]present address: Max-Planck-Institute of Biochemistry, Am Klopferspitz 18, 82152 Martinsried, Germany
[*]gcnelso1@asu.edu

Abstract: Reliable sample delivery is essential to biological imaging using X-ray Free Electron Lasers (XFELs). Continuous injection using the Gas Dynamic Virtual Nozzle (GDVN) has proven valuable, particularly for time-resolved studies. However, many important aspects of GDVN functionality have yet to be thoroughly understood and/or refined due to fabrication limitations. We report the application of 2-photon polymerization as a form of high-resolution 3D printing to fabricate high-fidelity GDVNs with submicron resolution. This technique allows rapid prototyping of a wide range of different types of nozzles from standard CAD drawings and optimization of crucial dimensions for optimal performance. Three nozzles were tested with pure water to determine general nozzle performance and reproducibility, with nearly reproducible off-axis jetting being the result. X-ray tomography and index matching were successfully used to evaluate the interior nozzle structures and identify the cause of off-axis jetting. Subsequent refinements to fabrication resulted in straight jetting. A performance test of printed nozzles at an XFEL provided high quality femtosecond diffraction patterns.

References and links

1. B. W. J. McNeil and N. R. Thompson, "X-ray free-electron lasers," Nat. Photonics **4**(12), 814–821 (2010).
2. H. N. Chapman, P. Fromme, A. Barty, T. A. White, R. A. Kirian, A. Aquila, M. S. Hunter, J. Schulz, D. P. DePonte, U. Weierstall, R. B. Doak, F. R. N. C. Maia, A. V. Martin, I. Schlichting, L. Lomb, N. Coppola, R. L. Shoeman, S. W. Epp, R. Hartmann, D. Rolles, A. Rudenko, L. Foucar, N. Kimmel, G. Weidenspointner, P. Holl, M. Liang, M. Barthelmess, C. Caleman, S. Boutet, M. J. Bogan, J. Krzywinski, C. Bostedt, S. Bajt, L. Gumprecht, B. Rudek, B. Erk, C. Schmidt, A. Hömke, C. Reich, D. Pietschner, L. Strüder, G. Hauser, H. Gorke, J. Ullrich, S. Herrmann, G. Schaller, F. Schopper, H. Soltau, K. U. Kühnel, M. Messerschmidt, J. D. Bozek, S. P. Hau-Riege, M. Frank, C. Y. Hampton, R. G. Sierra, D. Starodub, G. J. Williams, J. Hajdu, N. Timneanu, M. M. Seibert, J. Andreasson, A. Rocker, O. Jönsson, M. Svenda, S. Stern, K. Nass, R. Andritschke, C. D. Schröter, F. Krasniqi, M. Bott, K. E. Schmidt, X. Wang, I. Grotjohann, J. M. Holton, T. R. M. Barends, R. Neutze, S. Marchesini, R. Fromme, S. Schorb, D. Rupp, M. Adolph, T. Gorkhover, I. Andersson, H. Hirsemann, G. Potdevin, H. Graafsma, B. Nilsson, and J. C. H. Spence, "Femtosecond X-ray protein nanocrystallography," Nature **470**(7332), 73–77 (2011).

3. J. C. Spence, U. Weierstall, and H. N. Chapman, "X-ray lasers for structural and dynamic biology," Rep. Prog. Phys. **75**(10), 102601 (2012).
4. J. Tenboer, S. Basu, N. Zatsepin, K. Pande, D. Milathianaki, M. Frank, M. Hunter, S. Boutet, G. J. Williams, J. E. Koglin, D. Oberthuer, M. Heymann, C. Kupitz, C. Conrad, J. Coe, S. Roy-Chowdhury, U. Weierstall, D. James, D. Wang, T. Grant, A. Barty, O. Yefanov, J. Scales, C. Gati, C. Seuring, V. Srajer, R. Henning, P. Schwander, R. Fromme, A. Ourmazd, K. Moffat, J. J. Van Thor, J. C. H. Spence, P. Fromme, H. N. Chapman, and M. Schmidt, "Time-resolved serial crystallography captures high-resolution intermediates of photoactive yellow protein," Science **346**(6214), 1242–1246 (2014).
5. A. M. Gañán-Calvo, "Generation of steady liquid microthreads and micron-sized monodisperse sprays in gas streams," Phys. Rev. Lett. **80**(2), 285–288 (1998).
6. D. P. DePonte, U. Weierstall, D. Starodub, K. Schmidt, J. C. H. Spence, and R. B. Doak, "Gas dynamic virtual nozzle for generation of microscopic droplet streams," J. Phys. D Appl. Phys. **41**(19), 195505 (2008).
7. D. P. Deponte, J. T. McKeown, U. Weierstall, R. B. Doak, and J. C. H. Spence, "Towards ETEM serial crystallography: Electron diffraction from liquid jets," Ultramicroscopy **111**(7), 824–827 (2011).
8. U. Weierstall, D. James, C. Wang, T. A. White, D. Wang, W. Liu, J. C. H. Spence, R. Bruce Doak, G. Nelson, P. Fromme, R. Fromme, I. Grotjohann, C. Kupitz, N. A. Zatsepin, H. Liu, S. Basu, D. Wacker, G. W. Han, V. Katritch, S. Boutet, M. Messerschmidt, G. J. Williams, J. E. Koglin, M. Marvin Seibert, M. Klinker, C. Gati, R. L. Shoeman, A. Barty, H. N. Chapman, R. A. Kirian, K. R. Beyerlein, R. C. Stevens, D. Li, S. T. A. Shah, N. Howe, M. Caffrey, and V. Cherezov, "Lipidic cubic phase injector facilitates membrane protein serial femtosecond crystallography," Nat. Commun. **5**, 3309 (2014).
9. C. E. Conrad, S. Basu, D. James, D. Wang, A. Schaffer, S. Roy-Chowdhury, N. A. Zatsepin, A. Aquila, J. Coe, C. Gati, M. S. Hunter, J. E. Koglin, C. Kupitz, G. Nelson, G. Subramanian, T. A. White, Y. Zhao, J. Zook, S. Boutet, V. Cherezov, J. C. H. Spence, R. Fromme, U. Weierstall, and P. Fromme, "A novel inert crystal delivery medium for serial femtosecond crystallography," IUCrJ **2**(Pt 4), 421–430 (2015).
10. A. Echelmeier, G. Nelson, B. G. Abdallah, D. James, S. Roy-Chowdhury, A. Tolstikova, V. Mariani, R. A. Kirian, D. Oberthüer, K. Dörner, P. Fromme, H. N. Chapman, U. Weierstall, J. C. H. Spence, and A. Ros, "Biphasic Droplet-Based Sample Delivery of Protein Crystals for Serial Femtosecond Crystallography with an X-Ray Free Electron Laser," 19th µTAS Proc **2015**, 1374–1376 (2015).
11. L. Rayleigh, "On the Capillary Phenomena of Jets," Proc. R. Soc. Lond. **29**(196-199), 71–97 (1879).
12. U. Weierstall, J. C. H. Spence, and R. B. Doak, "Injector for scattering measurements on fully solvated biospecies," Rev. Sci. Instrum. **83**(3), 035108 (2012).
13. R. B. Doak, D. P. DePonte, G. Nelson, F. Camacho-Alanis, A. Ros, J. C. H. Spence, and U. Weierstall, "Microscopic linear liquid streams in vacuum: Injection of solvated biological samples into X-ray free electron lasers," AIP Conf. Proc. **1501**, 1314–1323 (2012).
14. M. Trebbin, K. Krüger, D. DePonte, S. V. Roth, H. N. Chapman, and S. Förster, "Microfluidic liquid jet system with compatibility for atmospheric and high-vacuum conditions," Lab Chip **14**(10), 1733–1745 (2014).
15. K. R. Beyerlein, L. Adriano, M. Heymann, R. Kirian, J. Knoška, F. Wilde, H. N. Chapman, and S. Bajt, "Ceramic micro-injection molded nozzles for serial femtosecond crystallography sample delivery," Rev. Sci. Instrum. **86**(12), 125104 (2015).
16. J. Mačiulaitis, M. Deveikytė, S. Rekštytė, M. Bratchikov, A. Darinskas, A. Šimbelytė, G. Daunoras, A. Laurinavičienė, A. Laurinavičius, R. Gudas, M. Malinauskas, and R. Mačiulaitis, "Preclinical study of SZ2080 material 3D microstructured scaffolds for cartilage tissue engineering made by femtosecond direct laser writing lithography," Biofabrication **7**(1), 015015 (2015).
17. R. M. Felfel, L. Poocza, M. Gimeno-Fabra, T. Milde, G. Hildebrand, I. Ahmed, C. Scotchford, V. Sottile, D. M. Grant, and K. Liefeith, "In vitro degradation and mechanical properties of PLA-PCL copolymer unit cell scaffolds generated by two-photon polymerization," Biomed. Mater. **11**(1), 015011 (2016).
18. M. Farsari, S. Huang, P. Birch, F. Claret-Tournier, R. Young, D. Budgett, C. Bradfield, and C. Chatwin, "Microfabrication by use of a spatial light modulator in the ultraviolet: experimental results," Opt. Lett. **24**(8), 549–550 (1999).
19. M. Farsari, F. Claret-Tournier, S. Huang, C. R. Chatwin, D. M. Budgett, P. M. Birch, R. C. D. Young, and J. D. Richardson, "A novel high-accuracy microstereolithography method employing an adaptive electro-optic mask," J. Mater. Proc. Tech. **107**(1), 167–172 (2000).
20. Y. Zhang, Q. Chen, H. Xia, and H. Sun, "Designable 3D nanofabrication by femtosecond laser direct writing," Nano Today **5**(5), 435–448 (2010).
21. M. Malinauskas, M. Farsari, A. Piskarskas, and S. Juodkazis, "Ultrafast laser nanostructuring of photopolymers: A decade of advances," Phys. Rep. **533**(1), 1–31 (2013).
22. See specifications at http://www.nanoscribe.de
23. J. M. Montanero, A. M. Gañán-Calvo, A. J. Acero, and E. J. Vega, "Micrometer glass nozzles for flow focusing," J. Micromech. Microeng. **20**(7), 075035 (2010).
24. A. Rack, T. Weitkamp, S. Bauer Trabelsi, P. Modregger, A. Cecilia, T. dos Santos Rolo, T. Rack, D. Haas, R. Simon, R. Heldele, M. Schulz, B. Mayzel, A. N. Danilewsky, T. Waterstradt, W. Diete, H. Riesemeier, B. R. Müller, and T. Baumbach, "The micro-imaging station of the TopoTomo beamline at the ANKA synchrotron light source," Nucl. Instrum. Methods Phys. Res. **267**(11), 1978–1988 (2009).
25. D. Paganin, S. C. Mayo, T. E. Gureyev, P. R. Miller, and S. W. Wilkins, "Simultaneous phase and amplitude extraction from a single defocused image of a homogeneous object," J. Microsc. **206**(1), 33–40 (2002).

26. M. Vogelgesang, T. Farago, T. F. Morgeneyer, L. Helfen, T. dos Santos Rolo, A. Myagotin, and T. Baumbach are preparing a manuscript to called "Real-time Image Processing and Reconstruction for Synchrotron Experiments."
27. U. Weierstall, "Liquid sample delivery techniques for serial femtosecond crystallography," Philos. Trans. R. Soc. Lond. B Biol. Sci. **369**(1647), 20130337 (2014).

1. Introduction

1.1 Sample delivery in serial femtosecond crystallography

With peak intensities that are $10^8 – 10^{10}$ times greater than those of synchrotron sources [1] and the ability to out-run radiation damage, the X-ray free electron laser (XFEL) has enabled novel methodological advances in protein crystallography using serial femtosecond crystallography (SFX) [2,3]. Using a liquid stream containing micron or submicron sized hydrated protein crystals running across a pulsed hard X-ray laser beam, snapshot X-ray diffraction patterns from protein microcrystals are recorded and read out at 120 Hz, facilitating sub-picosecond time-resolved diffraction studies at room temperature [4]. Sample delivery in SFX therefore requires transporting millions of sensitive protein crystals of submicron dimensions, often in high vacuum, across the pathway of the pulsed X-ray beam. This can be achieved using a liquid jet formed in a Gas Dynamic Virtual Nozzle (GDVN), which focuses a liquid stream of a suitable buffer solution containing the crystals into the X-ray beam. The sample delivery requirement for SFX is to use a physical nozzle large enough to avoid clogging by bioparticles, yet fine enough to match the diameter of the X-ray beam focus, which is about 1 micron. As demonstrated by Gañán-Calvo [5] and later refined for SFX by DePonte et al. [6], this can be achieved by using an outer high pressure coaxial gas sheath to speed up a liquid stream through gas focusing to produce a much finer liquid stream than the physical nozzle diameter. Unlike conventional solid-walled nozzles, the walls that determine the jet diameter of this "virtual" nozzle are replaced by the sheath gas, which can reduce the jet diameter by a factor of 10 or more because of shear and pressure forces. Consequently, the GDVN can deliver a steady supply of hydrated sample in vacuum for many hours without clogging. Liquid jets of between 2 and 5 microns in diameter are routinely achieved. Submicron jets down to about 0.3 microns in diameter have been demonstrated [7], which are of importance to the development of single-particle imaging methods. This system has also proven ideal for pump-probe time-resolved X-ray diffraction [4], and several promising schemes are under development to reduce protein consumption by eliminating the protein that runs to waste between X-ray pulses [8–10].

GDVNs commonly consist of one glass capillary situated concentrically inside another [Fig. 1]. The distal end of the inner capillary is tapered and carefully positioned with respect to converging inner walls near the end of the outer capillary. Protein solution is driven with gas pressure through the inner capillary while high-pressure gas (typically helium) is fed into the interstitial space. The large pressure difference between the inside of the nozzle and the surrounding environment ensures a choked-flow condition at the gas aperture whereby the helium gas undergoes nearly sonic expansion that is largely unaffected by the environmental pressure. Due to mass conservation and the incompressibility of the liquid, the mass flow rate is constant, and the liquid must accelerate. The accelerating liquid jet leaves the end of the outer glass capillary as a freely suspended continuous stream that subsequently breaks up into droplets due to the Rayleigh – Plateau instability [11] [Fig. 1].
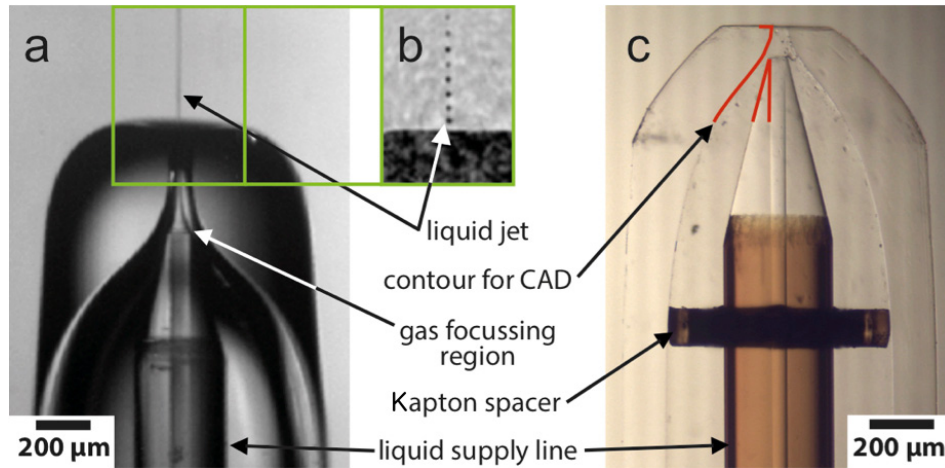
Fig. 1. (a) Bright field microscopy image from a traditional GDVN fabricated from flame polished glass capillaries. (b) Inset stroboscopic image of triggered droplets. (c) Image of nozzle components when immersed into an index-matched medium (glycerol), showing an undistorted view of the gas aperture profile and inner capillary position, as well as a laser-cut Kapton spacer for centering. The end of the outer glass capillary has been ground to a bevel to allow unshadowed wide angle X-ray diffraction. The contour indicated by the red line was used to derive the CAD model for the 3D printed nozzle.

1.2 Improved nozzles through 3D microfabrication

Traditional GDVN fabrication begins by melting the end of the outer glass capillary with a flame to form the converging inner profile that chokes the gas flow. The capillary end is then ground with an abrasive polishing disk to create a beveled exterior that allows for wide-angle x-ray diffraction without shadowing the diffracted radiation [Fig. 1(c)]. The opposite end of this outer capillary is inserted into a 5 cm section of stainless steel tubing and glued in place, such that the gas aperture protrudes from the end by several millimeters. The distal end of the smaller glass capillary, which is commercially coated with polyimide to prevent fracturing, is ground until it forms a truncated cone with a sharp rim. This end is inserted into the outer capillary and carefully positioned. Axial centering of the inner capillary is accomplished either with small, laser-cut Kapton supports or by using an outer capillary with a square inner cross section. In the latter case the flame polished end transitions from a square to a circular cross section, allowing the round conical tip of the inner capillary to be wedged in place without sealing off the gas flow [6,12].

This manual fabrication yields nozzles with variable jetting characteristics and limits scaling up of production. Each handmade nozzle is unique and careful testing is often required to validate assembled nozzles for use at a beamtime. Furthermore, flame polishing and grinding glass capillaries limits design versatility and capacity for ongoing nozzle development, e.g. micromixing and on-demand delivery for reduction of protein consumption. Hence, other microfabrication techniques are highly desired to improve resolution, repeatability, and yield. For example GDVN injectors fabricated through soft-litography in polydimethylsiloxane (PDMS) have been demonstrated [13,14]. However, soft lithography is essentially limited to planar, multilayered structures that may not be sufficiently robust for the high- and low-pressure extremes of SFX. Also, injection molding with sintering has been used to form a strong, high-resolution ceramic outer gas aperture [15]. Yet, injection molding is generally limited to purely convergent inner profiles without cavities. An ideal fabrication method can build all critical GDVN components in a robust material using a single process to an arbitrarily designed shape. Recent advances in femtosecond direct laser writing now offer the ability to write both the internal and external GDVN-sized structures at high resolution in robust polymer materials in an arbitrarily three

dimensional geometry within hours [16,17]. By utilizing a 2-photon polymerization (2PP) process, it enables 3D printing of microstructures with a resolution well beyond other high-resolution 3D printing technologies like UV laser microstereolithography, for instance [18,19]. This is achieved by tightly focusing a laser into a photosensitive material, and only in a small region near the focus is the light intensity high enough to trigger a non-linear light absorption process that photopolymerizes and hence solidifies the material locally. Sub-100 nm spatial resolution has been shown, and by moving the absorbing medium relative to the laser or vice versa in a precise and controlled manner, complex 3D high-resolution structures are realized [20,21].

In this study, we 3D printed nozzle tips using the Photonic Professional GT (Nanoscribe GmbH, Karlsruhe, Germany) [22]. Submicron resolution printing was performed within many 400 x 400 x 10 μm^3 (or smaller) units that were stitched together to form a 3D printed GDVN with a total volume of about 1 mm^3 in less than four hours.

For a basic test of functionality, two nozzles were printed using different photoresists: IP-S and IP-L. Following these tests IP-S was selected as the medium for an additional set of nine nozzles and printed successively over a single weekend to test for reproducibility. Index-matching optical microscopy [23] and X-ray tomography were used to analyze the internal structure of the nozzles. Protocols were adjusted to improve fabrication, and additional nozzles were printed for additional jetting performance tests. Nozzles were also used in serial crystallography experiments using the X-ray beam at the Linac Coherent Light Source (LCLS) XFEL at SLAC to collect X-ray diffraction patterns.

2. Fabrication

2.1 Nozzle design

We designed our nozzle for 3D printing using AutoCAD 2014 (Autodesk, Mill Valley, CA) to match the profile of the reference GDVN, which was fabricated using traditionally polished glass capillaries shown in Fig. 1 and known to produce a straight and steady jet. Jet formation and stability are most affected by the shape and relative position of the inner and outer nozzle housing near the exit orifice. We thus digitized line segments from one side of the profile of the reference GDVN and then revolved them around the flow axis into a 3D geometry. We added rib-like supports to firmly center the inner nozzle and entry ports to receive capillaries for liquid and gas supply. To minimize printing time, we made the nozzle as small as possible, while leaving orifice walls thick enough to withstand high gas and liquid pressures and the ports large enough to feasibly connect liquid and gas supply lines. The final nozzle design had a diameter and height of about 1 mm each [Fig. 2].

A prior fabrication trial indicated that for an annular array of 8 rectangular gas channels (each with a beginning hydraulic diameter of 70 μm^2, ending hydraulic diameter of 55 μm^2, and length of 675 μm) and a straight-bore central liquid channel of 50 μm^2 circular cross section and 477 μm length, at least 50 minutes of development in acetone was required to remove enough uncured photoresist for helium gas and water to traverse the channel system. Several design characteristics were subsequently included to ensure good access of the developer into the internal structure to fully develop uncured resin out of the internal volume, while also minimizing the required development time [Fig. 2]. A 50-μm inner / 150-μm outer diameter capillary with a cone profile was used to minimize the length of the inner channel of the printed nozzle, while maximizing the volume of the surrounding gas cavity (in prior trials, a 50-μm inner / 360-μm outer diameter capillary with a flat face was used). The lower end of the inner nozzle housing was tapered to form a bulb-like profile. To avoid trapping photoresist within the gas cavity and the inner capillary receiving port, three semicircular voids were included in the cylindrical sidewall of the outer housing, and the base of the inner nozzle housing was elevated above the substrate. The outer nozzle hull was tethered to the

inner nozzle housing with two sets of supports. Each set consists of three support ribs positioned 120° apart with respect to the central axis.
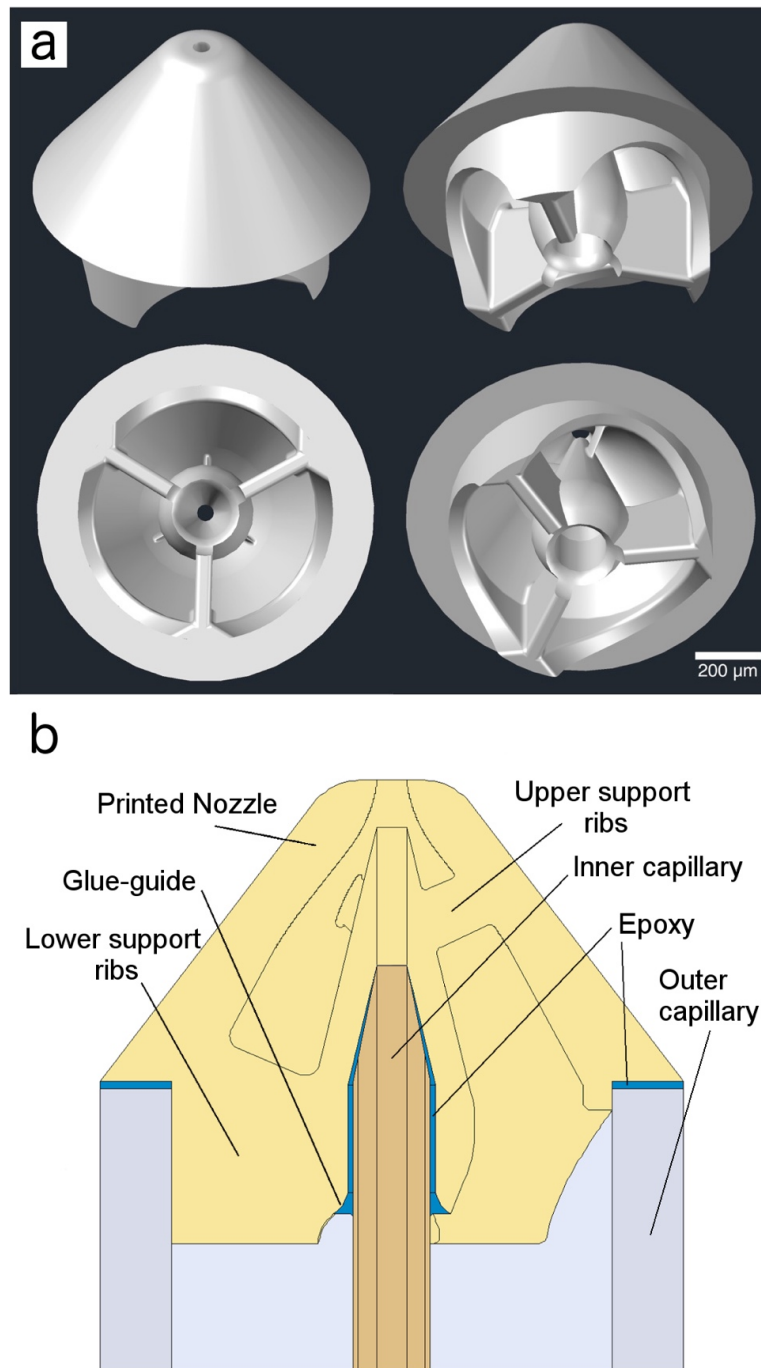

Fig. 2. (a) CAD renderings of nozzle design. (b) Cross section diagram of the printed nozzle tip assembly with both inner and outer capillaries glued into place.

A fillet around the entrance of the inner capillary receiving port provides a "glue-guide". After the liquid supply capillary is inserted, this recess provides a pathway for a droplet of

epoxy to be drawn completely around the capillary through capillary action, bypassing any need for multiple applications of glue and/or complicated movement by the applicator, nozzle, or capillary structures.

The overhanging structure that rests upon the outer capillary abutment provides the stopping point for when the entire structure (including the glued-in sample capillary) is inserted into and glued to a tube to act as a carrier for gas to flow coaxially around the inner capillary. The diameter of the cylindrical base was made to match the inner diameter of the gas transport tube, so that ideally the inserted nozzle would be held in place by friction while gluing.

The buoyancy of cured resin can result in the dislocation of printed features if the stiffness of the printed geometry is not sufficient to resist flexing. A printing simulation was performed using the native software of the Photonic Professional GT to identify and correct for free-floating structures that would occur during the printing process. With the exception of the abutment described above, unwanted flexing of printed materials was prevented by including fillets throughout the design to provide a continuous transition from vertical to horizontal geometries. The fillets also functioned to increased the overall strength of the printed nozzle and to provide more favorable gas flow.

2.2 3D printing

The 3D nozzle geometry, defined in STL file format, was converted into a print job file that specified required printer operations for fabrication using NanoWrite (Nanoscribe GmbH, Karlsruhe, Germany). A set of nine nozzles were printed on the Photonic Professional GT system using a 25x, NA = 0.8 objective lens with a slicing distance of 1 µm and hatching distance of 0.5 µm. In theory, the used objective lens illuminates a point spread function with a full width at half maximum of 0.6 µm in x-y and 3.4 µm in z. Overlap of voxels according to the printing parameters mentioned above resulted in submicron resolution printing with the exception of the stitched planes. The placement of units was chosen to prevent vertical stitching planes from intersecting the liquid flow axis. The preference of nozzles printed in IP-S resist over nozzles printed in IP-L resist was established when the inner nozzle housing of an IP-L resist nozzle became completely detached from the lower support ribs during the mounting process described below in section 2.5. The same mounting process was performed with nozzles formed in IP-S resist with no structural failure.

2.3 Nozzle development

IP-S nozzles were developed by incubation (unstirred) in mr-DEV 600 (micro resist technology GmbH, Berlin, Germany) for 10 minutes to solvate bulk IP-S resist situated around the nozzle. The nozzles were then transferred into fresh mr-DEV 600 and developed for 45 minutes followed by a 10 minute wash in an isopropanol bath. Nozzles were then allowed to dry on a clean glass surface in air for 10 minutes. Subsequent development-wash-dry cycles used the same solutions and incubation times, with the only addition of applying a 200 mBar vacuum during the first 15 minutes of the 45 minutes of the mr-DEV 600 development step. This was necessary to evacuate air pockets out of the internal geometry to allow for equal incubation of all internal structures.
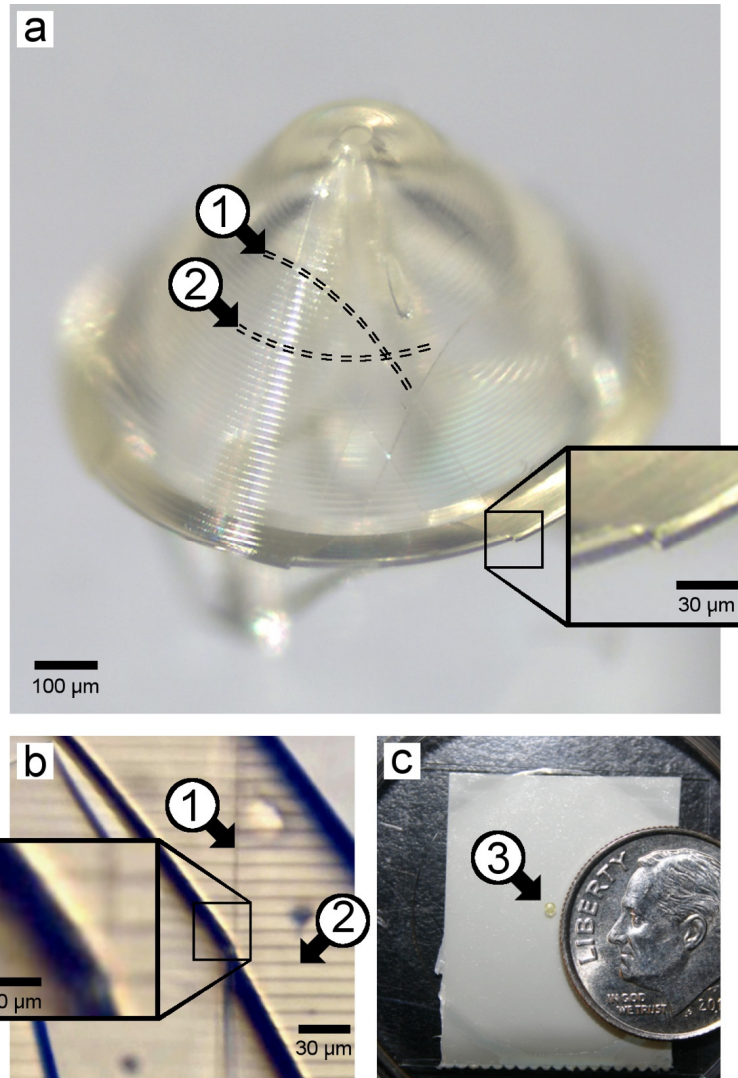
Fig. 3. (a) IP-S resist 3D printed GDVN. Stitching interfaces between the 400x400x10 μm^3 units are visible as vertical (arrow 1) and horizontal (arrow 2) slices through the device. Misalignment appears at the perimeter as magnified in the inset, presumably due to free-floating regions with no support underneath. (b) Index-matched image (nozzle immersed in glycerol) showing projection of both vertical (arrow 1) and horizontal (arrow 2) stitching lines, corresponding to those shown in (a). Horizontal and vertical stitching lines cause very little disruption to continuity of features on the inner sidewall (insert). (c) 3D printed GVDN next to a U.S. dime (arrow 3).

2.4 Nozzle imaging

The stitching interfaces between 400 x 400 x 10 μm^3 units were visible with optical microscopy as parabolic cross-sections through the cone of the nozzle and horizontal marks [Fig. 3(a)]. Bright field microscopy with index-matching by immersion in glycerol confirmed the 10-μm spacing and gave a projected view of both types of stitching with appropriate illumination [Fig. 3(b)]. The horizontal slices all look identical at this resolution. The submicron resolution printing within the 400 x 400 x 10 μm^3 units resulted in a smooth and continuous appearance with the exception of possible disruptions in the continuity of the sidewall profile appeared as shallow 1 to 2 μm-sized dips at the edge of each horizontal

stitched region [see inset of Fig. 3(b)]. Stitching errors around the circumference of the nozzle were more apparent, ranging from 1 to 5 μm [inset of Fig. 3(a)]. These errors were likely the result of upward buoyant flexing of the overhanging structure during printing [Fig. 4(d)], as opposed to inaccuracy of the printing system itself.
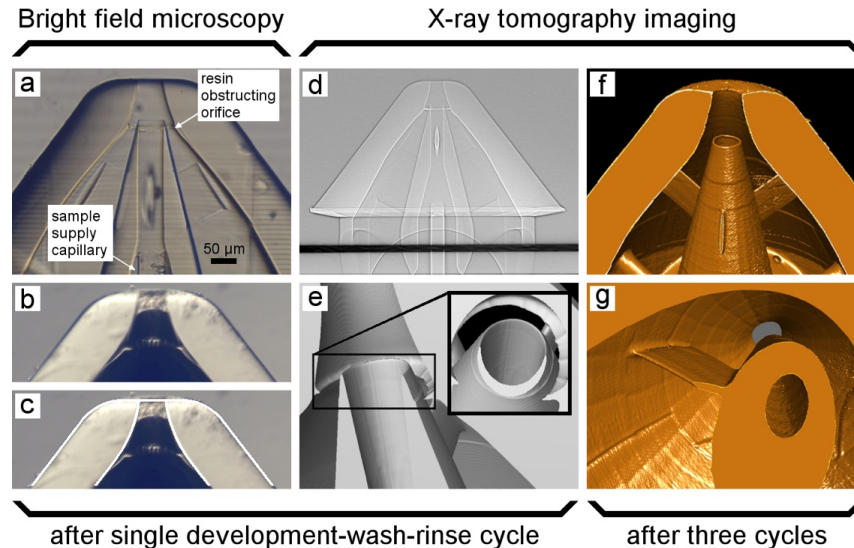

Fig. 4. Imaging of 3D printed nozzle tips to evaluate printing quality. (a) Bright field microscopy image of a fully assembled nozzle submerged in glycerol for index matching. A thin resin deposition is visible at the gas-focusing orifice. Also visible is the snug fit between the polished glass sample supply capillary and the 3D printed nozzle. (b) Nozzle tip submerged in glycerol with air bubble trapped inside. The original edge of the sidewall profile is clearly distinguishable from the deposition and matches the sidewall profile from the original CAD contour as highlighted by the white outline (c). (d) X-ray transmission image of a dried 3D printed nozzle after development. The black line at the bottom results from X-ray reflection of the glass substrate on which the nozzle was printed. (e) Cross sectional views from 3D surface rendering from an X-ray tomography reconstruction. The cutting plane of the cross section in each image is tilted with respect to the nozzle flow axis to illustrate the uneven resin accumulation near the tip in detail. (f, g) 3D surface rendering of nozzle after development with revised protocol (three development-wash-rinse cycles as opposed to just one). The nozzle was completely cleared of residual resin.

Inspection of nozzles using bright field microscopy in glycerol and X-ray tomography revealed a characteristic accumulation of material at the nozzle orifice, which was fully removed with a revised development protocol [Fig. 4]. In all nozzles imaged, an accumulation of material was obscuring the gas orifice to varying degrees [Fig. 4(a)-4(e)]. The original edge of the printed profile can be seen in the index-matched images, suggesting post-printing deposition and curing [Fig. 4(b)-4(c)]. To better deduce these depositions and their three dimensional extent at high resolution, we acquired full X-ray tomography data sets for three nozzle tips that were still adherent to the ITO glass printing substrate after development [Fig. 4(d)]. Initial tomography experiments were conducted at the TopoTomo beam line at ANKA, Karlsruhe, Germany [24] using a filtered white beam mode with 0.5 mm Aluminum, an indirect detector consisting of an Lu_2SiO_5 12 μm thick scintillating screen, 10x magnification objective lens and PCO.dimax camera with an effective pixel size of 1.22 μm. Resulting projections were flat field corrected to remove background defects before the phases were retrieved [25] to increase contrast. A filtered backprojection algorithm [26] was then used to reconstruct 3D volumes from the preprocessed projected thickness data. Obtained 3D reconstructions were analyzed as 3D surface renderings using VGstudio MAX software suite (Volume Graphics GmbH, Heidelberg, Germany). In all three tomographic nozzle reconstructions the depositions formed a similar aperture that fully surrounded the tip at the

narrowest section between inner and outer orifice [Fig. 4(e)]. In all cases these apertures had a pronounced acentric opening, likely resulting in uneven sheath gas flow. From the imaging we concluded that the depositions form after development when the developer solution is allowed to dry away. The evaporating droplet of developer solution remaining inside the nozzle tip likely becomes pinned to the narrow section between inner and outer orifice. While continuously shrinking this droplet can lower its overall surface tension by following the tapered structure until it has condensed into a thin enough sheet that can rupture spontaneously. Such a process would concentrate any amount of resin not yet solubilized in the internal nozzle structure into the thin wedge close to the orifice. To avoid this undesired deposition, we accordingly revised our development protocol to develop, wash and dry at least three times [Fig. 4(f) and 4(g)]. The tomogram of the nozzle tip after three development cycles was recorded at the Helmholtz-Zentrum Geesthacht operated PETRA III beamline P05 at DESY, Hamburg, Germany. The scan was performed in 1800 projections using a monochromatic x-ray beam at 14 keV in absorbtion contrast mode. With an effective pixel size of 660 nm and a 100 μm thick $CdWO_4$ scintillator a spatial resolution of ~1 μm was achieved.

2.5 Connecting sample lines

To interface our 3D printed nozzle tip we used a custom mounting stage with a PatchStar micromanipulator (Scientifica, East Sussex, UK) to glue the liquid and gas supply lines into place [Fig. 5(a) and 5(b)]. The 3D printed nozzle was held in place using vacuum tweezers that were fitted with a custom headpiece. A MicroTight union from IDEX was attached to an arm extending from the face of a 3-axis micrometer stage. After removing debris and liquid from the cone grinding process, the inner capillary was fed in reverse through the union and held in place with MicroTight fittings. With the vacuum tweezers holding the 3D printed nozzle in place, the distal end of the inner liquid capillary was inserted into the central receiving port of the printed nozzle using the micrometer stage. Once in place, the vacuum tweezer system was turned off.

By design there was a slight mismatch in angle between the inserted capillary cone and the cone profile of the receiving port. The angle of the capillary was chosen to be "sharper" to allow the glass tip of the inserted capillary to make hard contact with the nozzle structure at the capillary tip, providing a hard barrier to prevent glue from spilling over but allowing room for glue to optimally fill in the void.

A drop of fast-curing epoxy (Devcon or Hardman) was put in contact with the end of a hypodermic needle that was attached to the micromanipulator [Fig. 5(c)] so that a small glue sphere adhered to the needle tip. The needle tip was positioned near the gluing target with preprogrammed coordinates and then controlled manually for the gluing process.

The "glue guide" worked as intended and drew the epoxy completely around the inserted capillary using surface forces [Fig. 5(c)]. The glue finds its way around the capillary at a much faster rate than the rate at which it is drawn coaxially up the much smaller cavity between the capillary outer wall and the receiving port wall. Once the annulus is filled, the glue propagates upwards in an approximately uniform manner.

We have found experimentally that the size and shape of the glue guide has a bearing on the ease of application. With the glue on the end of an applicator forming naturally into a sphere, a concave-down curvature intersects with the incident glue sphere in a manner that assures the initial point of contact is within the glue guide. This is important since glue that is applied at unintended locations within the inner nozzle structure may affect nozzle performance. The epoxy bond between the sample capillary and the printed nozzle was allowed to fully cure overnight.
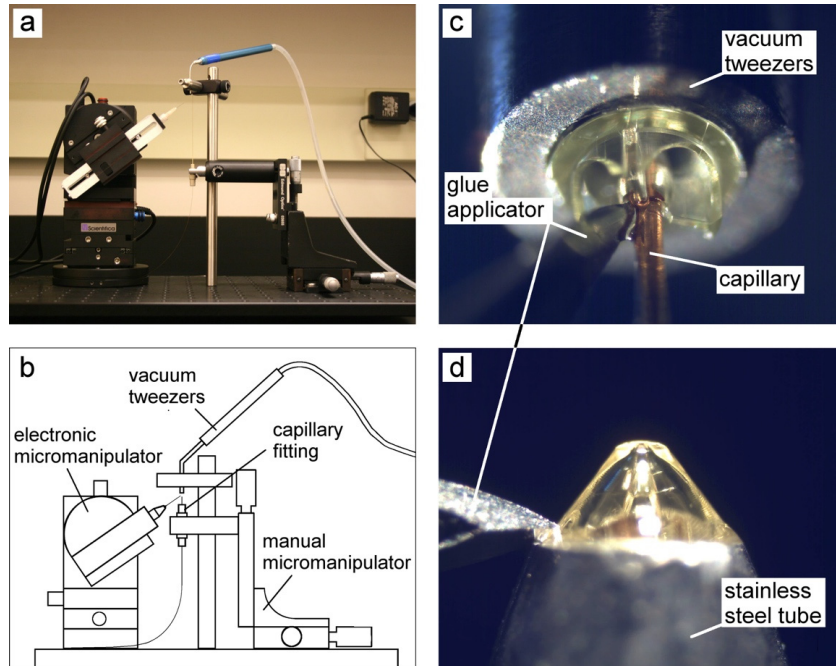
Fig. 5. (a) Photograph of mounting stage. (b) Diagram of mounting stage indicating the electronic micromanipulator with syringe needle applicator, vacuum tweezers apparatus, fitting for holding the sample capillary securely, and manual micromanipulator for positioning and inserting capillary into nozzle. (c) The 3D printed nozzle is held in place with the vacuum tweezers while the sample capillary is inserted. With the nozzle secured by the capillary the vacuum tweezers can be turned off, and the capillary is then glued in place by applying epoxy with an applicator that is connected to the electronic micromanipulator. (d) The 3D printed nozzle with the attached capillary is glued into a steeply beveled stainless steel tube.

The mounting stage was then modified slightly by replacing the vacuum tweezers with the gas transport tube, and then repositioning the apparatus that formerly held the vacuum tweezers so that the applicator needle could approach the nozzle directly from the side. Some nozzles were connected to stainless steel gas transport tubes, which had previously been given a steep bevel to match or exceed the nozzle angle. Stainless steel was chosen in lieu of glass to make the finished nozzle more robust against accidental breakage. However, other nozzles were connected to glass gas transport tubes, so that the inside was visible. The gas transport tubes were placed in the apparatus that formerly held the vacuum tweezers. The nozzle was then inserted into the distal end of the gas transport tube and ideally held in place by friction (although the nozzle was designed to match precisely with the stainless steel gas transport tubes, the inner diameter of the glass gas transport tubes did not match closely enough to hold the nozzles with friction and were much more difficult to glue). Epoxy was applied to the boundary using the micromanipulator [Fig. 5(d)], while the gas transport tube was rotated by hand. A second glass capillary was inserted into the proximal end of the gas transport tube to introduce the Helium sheath gas. Finally, the proximal end of the tube was sealed with epoxy in order to provide a gas-tight seal and to fix all capillaries in place. After the epoxy was fully cured, the stainless steel tube was attached to a standard GDVN holder, which in turn has connections to the nozzle rods used for in-vacuum sample injection [27].

3. Results

3.1 In-lab nozzle testing

Three nozzles from the initial set of nine nozzles were tested with pure water and helium gas to determine whether the printing resolution and symmetry were sufficient to produce a straight jet and to test whether the nozzles performed without fracturing. The minimum helium gas pressure and water flow rate that could be achieved without slipping from continuous jetting into a dripping mode was determined. These nozzles did not jet straight in either vacuum or atmosphere. A 100-µm inner diameter capillary of approximately 2 meters in length was used for the gas supply line with a minimum operational gas pressure for the 3D printed nozzles of about 50 psi as measured upstream of the supply capillary (300 to 500 psi is typical of handmade GDVNs). The minimum sample flow rate was 5 µl/min (5 to 20 µl/min is typical of handmade GDVNs).
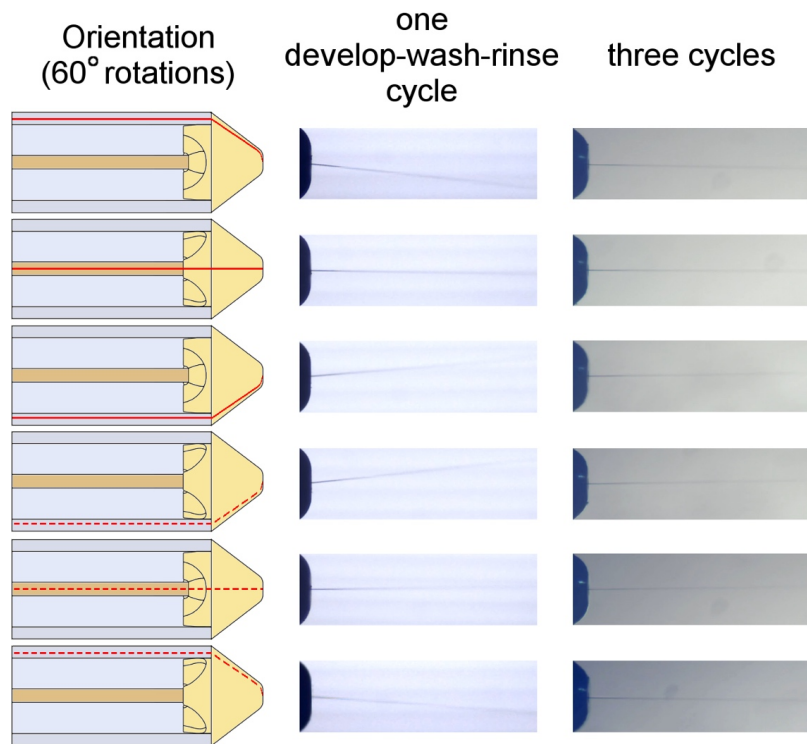

Fig. 6. Nozzle performance when jetting water in vacuum, comparing the use of one development-wash-rinse to the use of three cycles. An angular deviation of about 6° relative to the nozzle axis was observed when using one cycle, whereas when 3 cycles were used the measured angular deviation was less than 1°. Nozzles are rotated by 60° between subsequent images as indicated by the red line in the schematics on the left column.

Comparative views for the three nozzles were collected by taking videos of each nozzle jetting while rotating each GDVN holder around its flow axis. For these tests helium gas pressure, water flow rate, and supply capillary length were made as identical as possible by maintaining the helium gas regulator in a fixed position between nozzle changes, using an in-line digital liquid flow meter (Sensirion), and cutting the capillaries to equal lengths of 200 ± 1 cm. Bringing the gas supply capillaries to equal length was necessary to ensure equal flow resistance (i.e. equal gas mass flow rate) at the given pressure. It was necessary to refocus the microscope at times due to slight disagreement of the nozzle flow axis with the rotation axis. Imaging points during rotation were chosen at 60° intervals based on centering the cylindrical

outer sidewall of the nozzle as shown in Fig. 6. Corrective image rotations using image-editing software were performed so that the apparent nozzle cone angle was symmetric horizontally about the image window. Collections of these images as captured in sequence were compared side-by-side and matched according to the angular deviation of the jet from the nozzle axis. We found that the projected angle of the jet trajectory for the three nozzles varied one from another by no more than 2.5°, and each of these nozzles showed a maximum off-axis angle of about 6°.

A nozzle that was fabricated with the revised development procedure was connected to supply lines and tested with pure water. The resulting jet appeared straight and the gas pressure required for operation was comparable to the glass-based GDVN. Measurements were taken at 60° rotations, and a maximum off-axis angle of 0.9° was observed [Fig. 6].

3.2 Serial crystallography

Two of the off-axis-trajectory nozzles were used in serial femtosecond crystallography experiments (SFX) at the CXI endstation at the Linac Coherent Light Source (LCLS, a free-electron X-ray laser) to test whether the surface interaction of IP-S resist material with protein crystals preserves diffraction quality and to verify that the background signal from the IP-S resist material was sufficiently low for successful SFX data collection.

Figure 7(a) shows X-ray scattering from a glass capillary GDVN (red) compared to that from a 3D printed nozzle running the same sample solution (blue) and when no sample was running (green). The solid lines are mean radial intensities, with the shaded region bounded by the mean absolute deviation (MAD) from the mean. To compensate for potentially different liquid stream diameters between the printed nozzle and glass capillary GDVN, the mean radial intensity of the printed nozzle data were scaled by 0.5 to be equal to the glass capillary scattering at 2Å. Scattering from the printed nozzle is weak [green line in Fig. 7(a)], with a broad peak centered at ~5 Å. This additional background scattering (blue line) will not affect the integrated background-subtracted Bragg intensities in SFX data as the background is calculated locally around each Bragg spot. For a weak diffraction signal from a crystal, the background scattering from the printed nozzle would lead to a very slight decrease in the signal to noise ratio of peaks around 5Å resolution. For high intensity crystal diffraction spots, the decrease in the signal to noise ratio would be negligible. These intensities were collected minutes apart, with the same statistical fluctuations in the incident X-ray flux. The particularly large MAD values in the glass capillary GDVN data set are due to fluctuations in the thickness of the liquid stream intersected by the X-ray beam. The XFEL pulses had a mean energy of 8.7 keV, 40 fs duration, and the detector was 138 mm from the interaction region. Figure 8 shows a cytochrome *c* oxidase microcrystal diffraction pattern from these test runs, with sharp Bragg spots extending to 4 Å resolution.
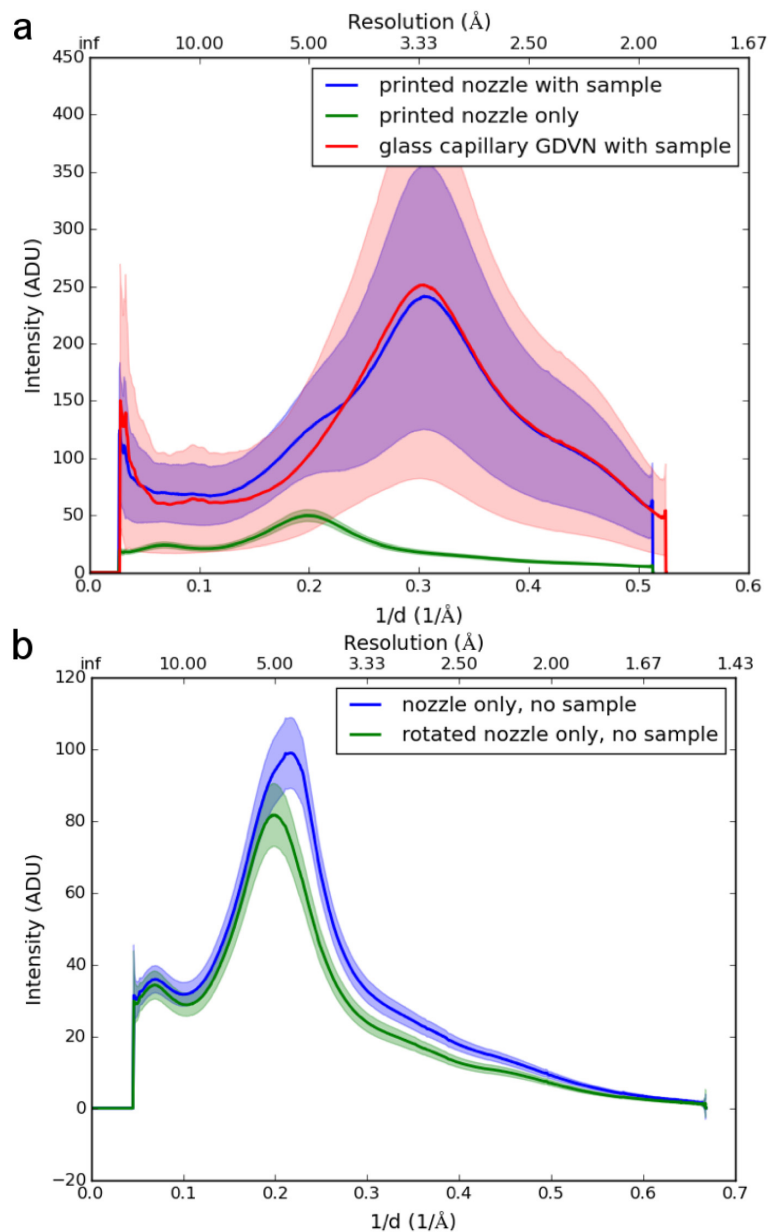
Fig. 7. (a) X-ray scattering from 3D printed nozzle with (blue) and without sample (green) compared to scattering from a glass capillary GDVN running the same sample (red). The mean radial intensities are plotted as solid lines. The shaded region is bounded by the mean absolute deviation from the mean. The broad peak centered on 3.3Å is from the aqueous buffer, and the small peak at ~5 Å is from the printed nozzle. (b) Background scattering from 3D printed nozzle without sample running, from 2 orientations of the nozzle, rotated by 30° about the nozzle axis.
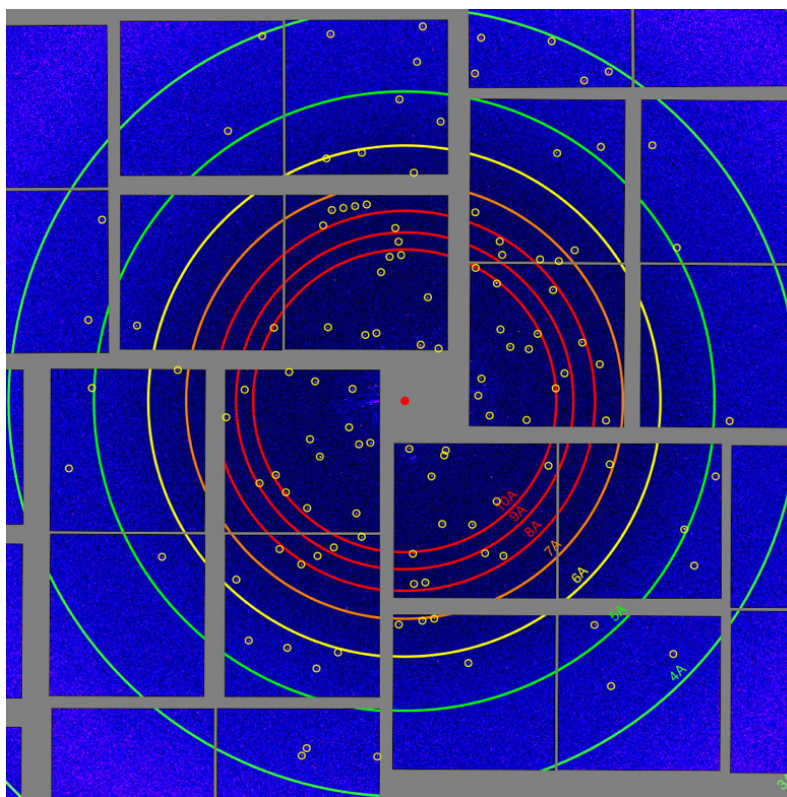
Fig. 8. Example of membrane protein (cytochrome *c* oxidase) crystal diffraction obtained using a 3D printed nozzle, with sharp Bragg spots extending to 4 Å. No difference was observed between the quality of diffraction from samples run in the printed nozzle compared to a glass capillary GDVN.

Figure 7(b) shows radial scattering profiles from the same printed nozzle in two orientations (rotated by 30° about the liquid flow axis), without liquid flowing. These measurements were obtained during a different LCLS experiment, at the same X-ray energy, but with a detector distance of 85 mm. The two orientations of the nozzle produce slight shifts in the resolution and intensity of the diffuse scattering peak from the nozzle, but neither orientation leads to strong scattering signals that would affect SFX data deleteriously.

4. Discussion and conclusions

Using 2PP we could 3D print functional GDVNs suitable for SFX sample delivery. The initial prints resulted in off-axis jetting and an unusually low operational range for the helium gas pressure. These constricted nozzles were successfully used in SFX experiments. The unusually low helium gas pressure range was beneficial in this case since a reduction in helium gas mass flow rate reduces the likelihood of damage to sensitive detector equipment in vacuum chambers that arises when helium levels are sufficiently high for electrical arcing to occur. Consequently, it may be worth intentionally printing an axially symmetric constriction in future designs. Through multiple development cycles we achieved complete development of the internal nozzle geometry and resulting in straight jetting at operating gas pressures within the typical range of hand-made glass GDVNs.

Index-matching and X-ray tomography proved to be complementary means for imaging interior nozzle structures to optimize nozzle design and fabrication. Index-matching clearly revealed the original sidewall profile beneath the suspected depositions, and X-ray tomography enabled exploration of the defect in detail. Glycerol index-matching was more

readily implemented than X-ray imaging, as only an optical microscope and glycerol medium was required, instead of access to a suitable X-ray facility. X-ray tomography in turn provided for a full 3D analysis of the internal nozzle geometry at higher resolution. Aside from improved resolution due to their shorter wavelength, imaging with X-rays compared to optical light is also much less sensitive to refractive index mismatches between nozzle resin, liquid sample and surrounding sheath gas. We hence anticipate X-ray radiography to enable unprecedented imaging of mixing dynamics and laminar flow regimes during liquid jet formation, which are difficult to quantify using standard optical or fluorescent microscopy.

In actual SFX sample delivery it was confirmed that the photoresist material itself did not adversely affect protein crystal diffraction. In most respects, the printed nozzle performance was no different than the performance of hand-ground glass GDVNs, while benefitting from the lower-than-normal helium gas pressure as described above. The successful acquisition of SFX diffraction implies that 2PP 3D printed nozzles can be a suitable alternative to conventional GDVN nozzles. Producing and testing a new design is straightforward and does not require new tooling, which in the case of injection molding may require several weeks to prepare. Hence, we anticipate the 2PP 3D printing to be very useful in complementing computer simulations of nozzle jetting to iteratively optimize a new nozzle design quickly.

A particularly intriguing feature of the 2PP 3D printing process is the ability to fabricate nested structures, which are difficult or even impossible to achieve in conventional glass capillary, injection mold, or soft lithography based GDVN nozzles. This ability to overcome geometry constraints imposed by traditional fabrication processes will facilitate the development of new types of injectors such as for solution scattering, single-particle imaging, mixing nozzles, flow focusing and pulsed jets. We demonstrated that repeated development-wash-rinse cycles are a suitable approach to develop internal structures, which should enable fabrication of more complex internal geometries in the future.

Further work is needed to optimize design features, printing conditions and resist development procedures to further improve printing speed, yield and overall jetting performance. Additional work includes eliminating the need for the micromanipulator-assisted assembly in this study. This may be achieved by directly printing nozzles to interface seamlessly with a standardized manifold for sample injection.

Acknowledgments